Journal of Materials Chemistry A

Accepted Manuscript

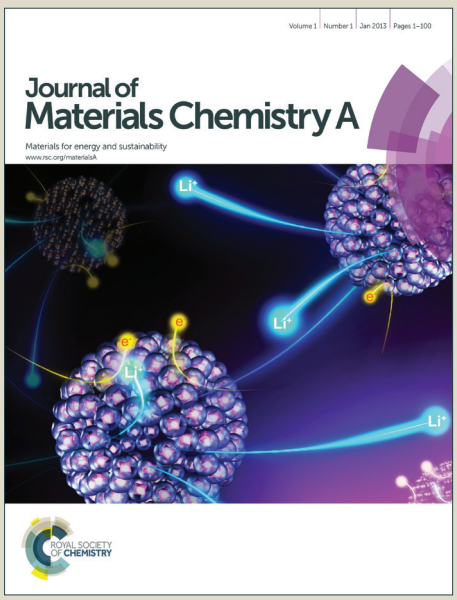

ROYAL SOCIETY OF CHEMISTRY

www.rsc.org/materialsA

Well-shaped Mn_3O_4 tetragonal bipyramids with good performance for lithium ion batteries

Taotao Li[a], Chunli Guo[a,], Bo Sun[b], Ting Li[a], Yonggang Li[a], Lifeng Hou[a]. Yinghui Wei[a,c,]**

[a.]College of Materials Science and Engineering, Taiyuan University of Technology, Taiyuan, Shanxi, 030024, P.R. China

[b.]Department of Mechanical Engineering, National University of Singapore, 119260, Singapore

[c.]Lvliang College, Lishi Shanxi 033000, China

*Corresponding author: Chunli Guo and Yinghui Wei, Tel./Fax: +86 351 6018683,

Email address: guochunli@tyut.edu.cn and weiyinghui@tyut.edu.cn

Abstract:

Well-shaped Mn_3O_4 tetragonal bipyramids with a high reversible capacity of 822.3 mA h g^{-1} are synthesized by a simple hydrothermal method without any surfactants or coordination compounds. The structural feature and morphology of the final product are investigated by X-ray diffraction (XRD), scanning electron microscopy (SEM) and high-resolution transmission electron microscopy (HRTEM). The SEM and HRTEM results reveal that all eight exposed facets of the Mn_3O_4 tetragonal bipyramids are indexed to the high-energy {101} planes. The tetragonal bipyramids with high-energy facets provide Mn_3O_4 anode material with high initial discharge capacity (1141.1 mA h g^{-1}). In addition, the anode displays good fast rate

performance, delivering a reversible capacity of 822.3 mA h g^{-1} (the theoretical capacity: 937 mA h g^{-1}) at a current density of 0.2 C after 50 cycles. And the coulomb efficiency for the first cycle reaches about 66% and remains at about 100% during the subsequent cycles. A relatively detailed growth mechanism of these tetragonal bipyramids is proposed in this manuscript.

Keywords:

Mn_3O_4 tetragonal bipyramids, {101} planes, lithium ion batteries

1. Introduction

Lithium ion batteries have captured significant attention because of their high power density (150 Wh kg^{-1}) and high energy density (400 Wh L^{-1}). [1-3] It exhibits great prospects in small portable applications including mobile phone, notebook computer, digital camera, and other fields such as submarine, aerospace, and electric vehicle. As is known, graphite-based materials as main lithium ion battery anodes have been industrialized. However, graphite-based materials have a limited theoretical specific capacity of 372 mA h g^{-1} and a quick capacity fade caused by the disintegration, which cannot meet the broad need of the high-energy applications. [4-6] Therefore, the alternative anode materials with higher energy capability are urgently needed. Nanomaterials have gradually attracted attention in the application of lithium ion batteries due to a very large specific surface area, a short ion diffusion path, a creep resistant and a high plasticity.

Nano-sized transition metal oxides have been also considered as the promising alternative anode materials owning to their high theoretical specific capacity (450 -

1500 mA h g-1). [7, 8] Among the transition oxides, Mn_3O_4 is worthy of exploiting, not only because of its high theoretical capacity of 937 mA h g^{-1}, but also its better properties of low toxic, low cost and abundance in nature. [9-11] In addition, Mn_3O_4 exhibits the better thermo-stability than graphite-based materials as the batteries are overcharged or charged at a high rate. [9, 12] It is generally accepted that with the lower redox potential renders the higher energy density anode materials. Mn_3O_4 with the lower redox potential (1.2 V), has been conserved to be more fascinating than other transition metals such as cobalt (2 V). [11, 13] Thus, much effort has been put into the area of Mn_3O_4 as anode materials in the past years.

In order to obtain the excellent properties of Mn_3O_4 nanoparticles, many researches focused on the size control and morphology control of Mn_3O_4 nanomaterials. For instance, mesoporous Mn_3O_4 nanotubes delivering a reversible capacity of 641 mA h g^{-1} at a high current density of 500 mA g^{-1} were reported by Bai. [13] Single crystalline Mn_3O_4 nano-octahedras were synthesized by a hydrothermal method and their electrochemical results show a charge capacity of 500 mA h g^{-1} at a current density of 50 mA g^{-1} and a charge capacity of 350 mA h g^{-1} when cycled at 500 mA g^{-1}. [14] Mn_3O_4 nano-octahedras prepared by the calcination of a Zn-Mn citrate complex can exhibit a reversible capacity of about 240 mA h g^{-1} at a high rate of 1000 mA g^{-1}. [15] Mn_3O_4 octahedral nanocrystals were also prepared by a hydrothermal method and their cycle performances exhibited a discharge capacity of 269 mA h g^{-1} at a current density of 500 mA g^{-1}. [16] The above-mentioned experimental results showed that there were still a certain distance far from the theoretical capacity of 937

mA h g^{-1}.

In this paper, we report a surfactant-free hydrothermal method to fabricate the well-shaped Mn_3O_4 tetragonal bipyramids with a high reversible capacity using $KMnO_4$ and $H_2C_2O_4 \cdot 2H_2O$ as raw materials at 200 ºC for 12 h. High-revolution transmission electron microscope (HRTEM) data indicated that eight exposed facets of the Mn_3O_4 tetragonal bipyramids were the {101} planes. The electrochemical performance of the Mn_3O_4 tetragonal bipyramids as anode material was evaluated by cyclic voltammograms (CV) and galvanostatic discharge-charge tests. The electrochemical results indicate that the Mn_3O_4 tetragonal bipyramids exhibit a high initial discharge capacity (1141.1 mA h g^{-1}) and deliver a reversible capacity of 822.3 mA h g^{-1} at a current density of 0.2 C after 50 cycles, which reaches ~88% of the theoretical capacity of manganese oxides. The coulomb efficiency for the first cycle reaches about 66% and remains at about 100% during the subsequent cycles. Finally, the formation mechanism of the Mn_3O_4 tetragonal bipyramids was discussed from the view of crystallography.

2. Experimental section

2.1 Synthesis of the Mn_3O_4 tetragonal bipyramids

$KMnO_{4s}$ and $H_2C_2O_4 \cdot 2H_2O$ (99 %) were purchased and used without a further purification. In a typical procedure, $KMnO_4$ (0.50 g) was completely dissolved in the 40mL KOH solution (0.01 M) to form a dark purple solution. $H_2C_2O_4 \cdot 2H_2O$ (0.86 g) was added to the above solution. Then the mixed solution was transferred into a Teflon-lined stainless steel autoclave (60 mL), which was subsequently sealed and

maintained at 200 ºC, for 10 h and then cooled to room temperature. The brownish red product was collected and washed with distilled water and absolute ethanol several times. Finally, the product was dried under vacuum at 60 ºC for several hours.

2.2 Characterization

The phase of the products was characterized by an X-ray powder diffraction (XRD) technique using a Bruker D8 advanced X-ray diffractometer equipped with graphite-monochromatized Cu-Kα radiation (Kα = 1.5418 Å). X-ray photoelectron spectroscopy (XPS) spectra of the synthesized Mn_3O_4 tetragonal bipyramids were obtained with an Axis Ultra, Kratos (UK) using monochromatic Al Ka radiation (150 W, 15 kV, and 1486.6 eV). Scanning electron microscopy (SEM) images were taken with a MIRA3 LMH scanning electron microscope. The TEM and HRTEM images were recorded using a JEOL-2100 high-resolution transmission electron microscope at an acceleration voltage of 200 kV.

2.3 Electrochemical measurements

The working electrodes for electrochemical properties were prepared with 70 wt% active materials of the Mn_3O_4 tetragonal bipyramids, 20 wt% conducting acetylene black, and 10 wt% carboxy methyl cellulose (CMC) binder in water. The slurry was pasted on a clean copper foil followed by drying in vacuum at 80 ºC for 12 h. The resulting foil was roll-pressed and cut into a disc. The Mn_3O_4 tetragonal bipyramid cells were fabricated using lithium foil as a counter electrode and a reference electrode, celgard 2400 as a separator, and a solution of 1 M $LiPF_6$ in a mixture of ethylene carbonate (EC) and dimethyl carbonate (DMC) (1:1 by volume) as an

electrolyte. The assembly of the cells was carried out in an argon-filled humidity-free glove box. The cells were charged and discharged from 0.01 to 3.0 V at different current rates (Land CT 2001A). CV profiles were obtained in the range of 0.01–3 V at a scanning rate of 0.1 mV s^{-1} from an electrochemical workstation (CHI-760).

3. Result and discussion

The as-prepared product was characterized by XRD (Fig. 1 and Fig. S1). In Fig. 1,almost all the diffraction peaks of the as-synthesized sample can be well indexed as the tetragonal structure for Mn_3O_4 with lattice parameters of a = b = 5.763 Å and c = 9.456 Å, which is in good agreement with the data reported in the JCPDS standard card (No. 89-4837, space group I41/amd (141)). The valence of the Mn_3O_4 was analyzed by X-ray photoelectron (XPS) test. The XPS spectra in Fig. S2 indicate that the Mn2p region consists of a spin-orbit doublet (L-S coupling) with binding energy of 652.9 eV ($Mn2p_{1/2}$) and 642.1 eV ($Mn2p_{3/2}$) for Mn_3O_4 tetragonal bipyramids, which is characteristic of a mixed-valence manganese system (Mn^{3+} and Mn^{2+}). [17]

A SEM image (Fig. 2a) shows that the morphologies of the final sample are the Mn_3O_4 tetragonal bipyramids. Fig. 2b is a high-magnification SEM image of the Mn_3O_4 tetragonal bipyramids. It can be clearly observed that the surfaces of the well-defined Mn_3O_4 tetragonal bipyramids are mostly smooth. The inset in Fig. 2b is an ideal geometrical model of the Mn_3O_4 tetragonal bipyramids. We defined the vertice of long axis (C_4) as A and the vertice of minor axis (C_2) of the Mn_3O_4 tetragonal bipyramids as B or C. To obtain a closer insight of the inner structure of the well-defined Mn_3O_4 tetragonal bipyramids, TEM was carried out. Figs. 2c and 2d are

a low-magnification and a high-magnification TEM images, respectively. From Fig. 2c, there are two kinds of morphologies including square and rhombus, which are slightly different from the results observed from SEM. The reason was that these two morphologies were the projections of tetragonal bipyramids from different prospective. The inset in Fig. 2c is an ideal geometrical model of the Mn_3O_4 tetragonal bipyramids from the view of A, whose projection is a square with a dark crossing (marked with the white arrows). If viewed from the midpoint of AB in the geometrical model of Fig. 2d, the projection of the Mn_3O_4 tetragonal bipyramid labeled with the white arrows can become a rhombus. Based on our limited SEM observation along with a low resolution survey, it is estimated that up to about 95% of the Mn_3O_4 tetragonal bipyramids and their average sizes (Heywood diameter) range from 80 to 160 nm.

To further investigate the detailed microstructure of the Mn_3O_4 tetragonal bipyramids, high-resolution TEM imaging was employed. Fig. 3a is a typical TEM image of a whole Mn_3O_4 tetragonal bipyramid and Fig. 3c and 3d are the corresponding simulated geometrical model images along different directions. The diffraction spots of SAED pattern in Fig. 3b is in a regular sequence, which is featured of the monocrystal. The facets are best revealed by the projection of the Mn_3O_4 tetragonal bipyramid along [010] orientation, parallel to which 4 of the 8 exposed facets are imaged edge-on Fig. 3a. The Miller indices of exposed faces of the Mn_3O_4 tetragonal bipyramids can be confirmed by a conjunction of the angles between the facets in Fig. 3a, whose borders can be recognized as the projection of

four {101} facets parallel to the [010] orientation.[18] The HRTEM images in Figs. 3e and 3f recorded from the white rectangle areas of Fig. 3a show continuous lattice fringes with lattice spacing of 0.49 nm, which corresponds to the {101} planes of Mn_3O_4. As shown in Fig. 3e, the angle of two opposite surfaces ((101) and (-101)) of 63° is measured, which is in good agreement with the angle marked with a black double-headed arrow in Fig. 3d. From Fig. 3f, it can be calculated that the angle between (-101) and (-10-1) is 117°, in accordance with the angle marked with a white double-headed arrow in Fig. 3f. Based on the above-mentioned crystal data, the crystal orientation relation to the morphology can be determined in Fig. 3c. Therefore, we drew a conclusion that the crystal facets at the surface of the Mn_3O_4 tetragonal bipyramids accord with {101} planes.

As an effort to explore the growth mechanism for this synthetic route, it is necessary to check out the morphology and structure of samples prepared at various reaction times while other conditions were kept the same. Fig. 4a shows a SEM image of the products synthesized at 4 h. From Fig. 4a, two distinct morphologies were observed. One is aggregated micron-sized cubic-shaped nanoparticles, the other is one-dimension nanocrystals. Further SEM structural analysis provides more pronounced evidence to inspect the morphology of the white rectangle area in Fig. 4a. Fig. 4b is the typical SEM image of the one-dimension nanocrystals. Rod-like structures with an average width of 45 nm and an aspect ratio of 4-20 have been clearly observed. Moreover, XRD data also show the presence of two major phases of $MnCO_3$ and MnOOH (Fig. S3). According to the related papers, the chemical

composition of aggregated micron-sized cubic-shaped nanoparticles was $MnCO_3$ [19] and the chemical constitution of rod-like structures was MnOOH. [20, 21] So the possible chemical reaction pathway involved in the range of 0 to 4 h can be written as follows:

$$KMnO_4 + H_2C_2O_4 + KOH \rightarrow MnCO_3 + MnOOH + KHCO_3 + H_2O \quad (1)$$

When the reaction time was increased to 6 h, Mn_3O_4 and MnOOH were indexed in corresponding XRD (Fig. S4). No obvious diffraction peaks of $MnCO_3$ were observed in the XRD pattern, which suggests that $MnCO_3$ phase was an intermediate product. This interesting finding shows that the stability of $MnCO_3$ was not as good as that of MnOOH in our reaction route. It's common knowledge that MnOOH phase was stable in a strong alkali solution (Fig. S5). The SEM image of Fig. S6 also gives evidence that the aggregated cubic-shaped $MnCO_3$ nanoparticles disappeared and the Mn_3O_4 tetragonal bipyramids emerged. When the reaction time was further increased from 6 to 8 h, the proportion of the Mn_3O_4 tetragonal bipyramids in the final products was on the increase (Fig. S7).When the reaction time was extended to 10 h, more than 95% Mn_3O_4 tetragonal bipyramids have been inspected in our sample. Consequently, the chemical reactions involved in the growth from 4 to 10 h could be described as follows:

$$MnCO_3 + 2\ MnOOH \rightarrow Mn_3O_4 + CO_2 + H_2O \quad (2)$$

The reaction from 4 to 10 h can be summarized as the reaction diagram (Fig. 5). The overall reaction can be formulated as follows:

$$KMnO_4 + H_2C_2O_4 + KOH \rightarrow Mn_3O_4 + CO_2 + KHCO_3 + H_2O \quad (3)$$

Further on, in order to elucidate the growth mechanism of these Mn_3O_4

tetragonal bipyramids, we proposed a hypothesis in the frame of a structural transformation from $MnCO_3$ and MnOOH to Mn_3O_4 on the basis of the above-mentioned reactions (Fig. 4c). As the structure of $MnCO_3$ was destroyed completely along with the escaping of CO_2, the dissociative Mn^{2+} entered into the tetrahedral sites of the defective MnOOH cell. Then, the Mn_3O_4 spinel structure was formed. Fig. 4d presents the crystal structure of the tetragonal Mn_3O_4 with two unit cells. It is clearly displayed that the Mn_3O_4 structure has a normal spinel structure with the Mn^{2+} ($4s^0 3d^5$) in the tetrahedral sites and the Mn^{3+} ($4s^0 3d^4$) in the elongated octahedral sites, [22, 23] which can be explained by Jahn-Teller effect. [24] In the octahedral complexes of Mn_3O_4, five 3d orbitals of Mn atom in the Mn_3O_4 crystal structure are divided into two types: one is t_{2g} orbital (d_{xy}, d_{zx} and d_{xy}), the other is e_g* orbital (d_z^2 and $d_{x^2-y^2}$). [25] And Mn^{3+} has a high-spin configuration of $(t_{2g})^3$ $(e_g*)^1$. Every t_{2g} orbital (d_{xy}, d_{yz} and d_{zx}) has a 3d electron and the d_z^2 orbital of the e_g* orbital is occupied by the remaining 3d electron (Fig. S8). [26] Four O^{2-} of the octahedral Mn_3O_4 complexes in the XY plane received a smaller repulsive force than two O^{2-} in the Z axe (Fig. S9), resulting in the structure distortion from the octahedrons to the elongated tetragonal bipyramids. Furthermore, there are not the compounds such as the surfactants and the coordination compounds which can affect the growth faces of the tetragonal bipyramids in our hydrothermal system. Accordingly, the final morphology of the as-prepared samples is consistent with its primary framework structure. Based on the HRTEM and SAED results, we can know that the elongated octahedron structure stacked along the {101} planes simultaneously.

The electrochemical properties of the as-obtained Mn_3O_4 tetragonal bipyramids were firstly evaluated by CV. Fig. 6 displays three CV curves of the cell with the Mn_3O_4 tetragonal bipyramids used as anode material under different cycles. In the first catholic scan, there were two weak peaks appeared at 1.01V (a) and 0.88V (b), which both vanished in the succeeding cycles. The peak (a) can be attributed to a reduction reaction ($Mn_3O_4 + 2Li^+ + 2e^- \rightarrow MnO + Li_2O$)[27] and the peak (b) can be ascribed to the formation of a solid electrolyte interphase (SEI) layer ($electrolyte + e^- + Li^+ \rightarrow SEI\,(Li)$) on the surface of the Mn_3O_4 tetragonal bipyramid electrode.[14, 28, 29] In addition, the strong peak located at 0.08V (c) is related to a reduction reaction of MnO ($MnO + Li^+ + 2e^- \rightarrow Mn\,(0) + Li_2O$).[28] During the next anodic process, one peak located at 1.33 V (d) was observed due to an oxidation reaction of the former-formed Mn and the decomposition of Li_2O.[30] In the second catholic cycle, the reduction peak shifts from 0.08 V (c) to 0.32 V (e) mainly due to an irreversible phase transformation. After the second cycle, the appearance of similar CV curves indicates a good reversibility of the electrochemical reactions of the Mn_3O_4 tetragonal bipyramid electrode. On basis of the above analysis results and the relative literature,[31-33] the entire reversible electrochemical mechanism of Mn_3O_4 on Li insertion and extraction can be summarized by the following equation:

$$Mn_3O_4 + 8\,Li^+ + 8\,e^- \leftrightarrow 3\,Mn + 4\,Li_2O$$

Fig. 7 exhibits the discharge and charge curves of the 1st, 2nd, 10th and 50th cycles for the Mn_3O_4 tetragonal bipyramid electrode cycled between 0.01 and 3 V at a current density of 0.2 C. In the first discharge curve (Li insertion), three distinctive

regions (a, b and c) related to different Li storage mechanisms are observed. The first short plateau (a) and the following sloped region (b) can be assigned to the reduction reaction from Mn_3O_4 to MnO and the formation of the SEI film on the electrode surface, respectively. The long plateau (c) was related to the reduction reaction from Mn^{2+} to Mn^0. [27] In the first charge curve, a slight slope recorded between 1.1 and 1.5 V can be regarded as the oxidation reaction from Mn^0 to Mn^{2+} or Mn^{3+}. [27] All these results were in accord with the CV test results. From the second cycle, the discharge plateau (d) of the Mn_3O_4 tetragonal bipyramid electrode shifts to about 0.5 V, indicating the irreversible formation of crystalline: metallic Mn and amorphous Li_2O matrix. [27] After the second cycle such as 10^{th} and 50^{th} cycle, the discharge and charge curves are similar. However, nearly 7 mol Li is stored per mole Mn_3O_4 with a total capacity of 822 mA h g^{-1} during the 50^{th} cycle, which is higher than that (760 mA h g^{-1}) of the 10^{th} cycle.

Fig. 8 shows the cycling performance and the columbic efficiency of the Mn_3O_4 tetragonal bipyramid electrode at the rate of 0.2 C from 0.01 to 3.0 V about 56 cycles. As shown in Fig. 8, the Mn_3O_4 tetragonal bipyramid electrode delivered an initial capacity of 1141.1 mA h g^{-1} and exhibited a first cycle columbic efficiency of 66.7 %. The large irreversible capacity loss (33.3 %) in the first cycle is very common for the transition metal oxides, the main reason is the formation of an SEI film by the degradation of the electrolyte ($\text{electrolyte} + e^- + Li^+ \rightarrow \text{SEI}(Li)$), the other is the transformation of irreversible phase (Mn nanoparticles and amorphous Li_2O matrix). [14, 15, 36]

In the second cycle, its capacity quickly decreased to 761.1 mA h g^{-1} with an increased columbic efficiency of nearly 100%. In the subsequent cycles, the capacity and the columbic efficiency both remained steady. However, the capacity from the 20^{th} to the 56^{th} cycle increased from 765.7 to 822.3 mA h g^{-1} gradually. The growing reversible capacity can be explained by an interfacial mechanism in which extra lithium is accommodated in these boundary regions between nano-sized Mn and Li_2O (In the reaction process, the size of these two products got smaller and the boundary regions increased.) via charge separation. [34, 35]

In order to evaluate the power capability of the Mn_3O_4 tetragonal bipyramid electrode, we investigate its rate performance at different current densities (Fig. 9). From Fig. 9, the reversible capacity gradually decreases as the current density increases. The specific capacities of 869, 798, 708 and 604 mA h g^{-1} are detected as the current density varies from 0.1, to 0.2, 0.5 and 1 C, respectively. Even at a current density as high as 2 C, the Mn_3O_4 tetragonal bipyramid electrode can still deliver an average specific capacity of 471 mA h g^{-1}, much higher than the theoretical specific capacity (372 mA h g^{-1}) of graphite-based anode materials. [37] When the current density was back to 0.1 C, an average capacity could be recovered to 883 mA h g^{-1}, which was a little higher than the capacity (856.3 mA h g^{-1}) at the initial rate of 0.1 C. The enhanced electrochemical performance of the as-synthesized Mn_3O_4 tetragonal bipyramids could be ascribed to its special structure. The nanoparticles provide large specific surface area ((101) facets), which improve the utilization of active material, and provide reduced transport pathways for lithium ions to transfer in and out easily.

The structure of the Mn_3O_4 tetragonal bipyramids lithium ion batteries has the ability to tolerate the volume deformation during discharge-charge process and maintain the stability of the Mn_3O_4 electrode. These may be responsible to the good performance for LIBs. [13, 36] Therefore, the Mn_3O_4 tetragonal bipyramid electrode with a good rate capacity can be regarded as a promising alternative anode material for lithium ion batteries.

4. Conclusion:

The Mn_3O_4 tetragonal bipyramids with a high reversible capacity (up to 822.3 mA h g^{-1}) were synthesized by the reaction of $KMnO_4$ and $H_2C_2O_4 \cdot 2H_2O$ in the alkali solution at 200 ºC for 12 h without any surfactants or coordination compounds. Inspection of the HRTEM and SAED data of the final products showed that the Mn_3O_4 tetragonal bipyramids were monocrystal and the elongated octahedron structure of the Mn_3O_4 tetragonal bipyramids stacked along the {101} planes. The CV and the galvanostatic discharge-charge test results showed that the Mn_3O_4 tetragonal bipyramid electrode could display a high initial discharge capacity of 1141.1 mA h g^{-1} and deliver a reversible capacity of 822.3 mA h g^{-1}, close to the theoretical capacity value of 937 mA h g^{-1}, at 0.2 C after 50 cycles. The coulomb efficiency could be nearly 100% after the first cycles. A growth mechanism of the Mn_3O_4 tetragonal bipyramids was proposed and accounted for the obtained experimental results very well.

Acknowledgments

The authors acknowledge the National Science Foundation of China (Grant No.

51001079, 21201129, 51374151), the Top Young Academic Leaders of Higher Learning Institutions of Shan Xi, the Doctoral Found of Ministry of Education of China (Grant No. 20091402110010), the China Postdoctoral Science Foundation (20100471586) and the National Natural Science Foundation of Shan Xi Province (2011011020-2, 2010021023-1, 2013011012-3).

References

[1] J. M. Tarascon, M. Armand, Nature, **2001**, 414, 359.

[2] P. G. Bruce, B. Scrosati, J. M. Tarascon, Angew. Chem. Int. Ed., **2008**, 47, 2930.

[3] S. Goriparti, E. Miele. F. D. Angelis, E. D. Fabrizio, R. P. Zaccaria, C. Capiglia, J. Power sources, **2014**, 257, 421.

[4] T. H. Kim, J. S. Park, S. K. Chang, S. Choi, J. H. Ryu, H. K. Song, Adv. Enegy Mater., **2012**, 2, 860.

[5] Y. Z. Jiang, M. J. Hu, D. Zhang, T. Z. Yuan, W. P. Sun, B. Xu, M. Yan, Nano Energy, **2014**, 5, 60.

[6] Z. C. Bai, N. Fan, C. H. Sun, Z. C. Ju, C. L. Guo, J. Yang, Y. T. Qian, Nanoscale, **2013**, 5, 2442.

[7] P. Poizot, S. Laruelle, S. Grugeon, L. Dupont, J. M. Tarascon, Nature, **2000**, 407, 496.

[8] Z. Q. Li, N. N. Liu, X. K. Wang, C. B. Wang, Y. X. Qi, L. W. Yin, J. Mater. Chem., **2012**, 22, 16640.

[9] J. Gao, M. A. Lowe, H. D. Abruña, Chem. Mater., **2011**, 23, 3223.

[10] Z. C. Bai, Z. C. Ju, C. L. Guo, Y T. Qian, B. Tang, S. L. Xiong, Nanoscale, 2014,

5, 3268.

[11] F. Han, D. Li, W. C. Li, C. Lei, Q. Sun, A. H. Lu, Adv. Funct. Mater., **2013**, 23, 1692.

[12] J. Jiang, Y. Y. Li, J. P. Liu, X. T. Huang, C. Z. Yuan, X. W. Lou, Adv. Mater., **2012**, 24, 5166.

[13] Z. C. Bai, N. Fan, Z. C. Ju, C. L. Guo, Y. T. Qian, B. Tang, S. L. Xiong, J. Mater. Chem. A, **2013**, 1, 10985.

[14] S. Z. Huang, J. Jin, Y. Cai, Y. Li, H. Y. Tan, H. E. Wang, G. V. Tendeloo, B. L. Su, Nanoscale, **2014**, 6, 6819.

[15] Q. Hao, J. P. Wang, C. X. Xu, J. Mater. Chem. A, **2014**, 2, 87.

[16] W. Xiao, J. S. Chen, X. W. Lou, CrystEngComm., **2011**, 13, 5685.

[17] V. A. M. Brabers, S. F. M. Van, P. S. A. Knapen, J. Solid State Chem., 1983, 49, 93.

[18] N. Tian, Z. Y. Zhou, S. G. Sun, Y. Ding, Z. L. Wang, Science, **2007**, 316, 732.

[19] S. Devaraj, H. Y. Liu, P. Balaya, J. Mater. Chem. A, **2014**, 2, 4276.

[20] C. C. Hu, Y. T. Wu, K. H. Chang, Chem. Mater., **2008,** 20, 2890.

[21] W. X. Zhang, Z. H. Yang, S. P. Tang, X. Z. Han, M. Chen, J. Cryst. Growth, **2004**, 263, 394.

[22] R. Regmi, R. Tackett, G. Lawes, J. Magn. Magn. Mater., **2009**, 321, 2296.

[23] Y. Li, H. Y. Tan, X. Y. Yang, B. Goris, J. Verbeeck, S. Bals, P. Colson, R. Cloots, G. V. Tendeloo, B. L. Su, Small, **2011**, 7, 475.

[24] H. Jahn, E. Teller, P. Roy. Soc. A, **1937**, 161, 220.

[25] L. Wang, Y. G. Shi, Z. Chen, Y. B. Qin, H. F. Tian, C. Ma, H. X. Yang, A. A. Belik, Solid State Commun., **2013**, 153, 71.

[26] R. Tackett, G. Lawes,B. C. Melot, M. Grossman, E. S. Toberer, R. Sehadri, Phys. Rev. B, **2007**, 76, 024409.

[27] M. A. Lowe, J. Gao, H. D. Abruña, J. Mater. Chem. A, **2013**, 1, 2094.

[28] L. Li, Z. P. Guo, A. J. Du, H. K. Liu, J. Mater. Chem., **2012**, 22, 3600.

[29] K. F. Zhong, X. Xia, B. Zhang, H. Li, Z. X. Wang, L. Q. Chen, J. Power Sources, **2010**, 195, 3300.

[30] D. Pasero, N. Reeves, A. R. West, J. Power Sources, **2005**, 141, 156.

[31] J. F. M. Oudenhoven, L. Baggetto, P. H. L. Notten, Adv. Energy Mater., **2011**, 1, 10.

[32] H. L. Wang, Y. Yang, Y. Y. Liang, G. Y. Zheng, Y. G. Li, Y. Cui, H. J. Dai, Energy Environ. Sci., **2012**, 5, 7931.

[33] T. Li, Y. Y. Wang, R. Tang, Y. X. Qi, N. Lun, Y. J. Bai, R. H. Fan, ACS Appl. Mater. Interfaces, **2013**, 5, 9470.

[34] D. P. Dubal, R. Holze, RSC Adv., **2012**, 2, 12096.

[35] L. Ji, H. Zheng, A. Ismach, Z. Tan, S. Xun, E. Lin, V. Battaglia, V. Srinivasan, Y. Zhang, Nano Energy, **2012**, 1, 164.

[36] Z. C. Bai, Z. C. Ju, C. L. Guo, Y. T. Qian, B. Tang, S. L. Xiong, Nanoscale, 2014, 5, 3268.

[37] X. L. Wu, Q. Liu, Y. G. Guo, W. G. Song, Electrochem. Commun., **2009**, 11, 1468.

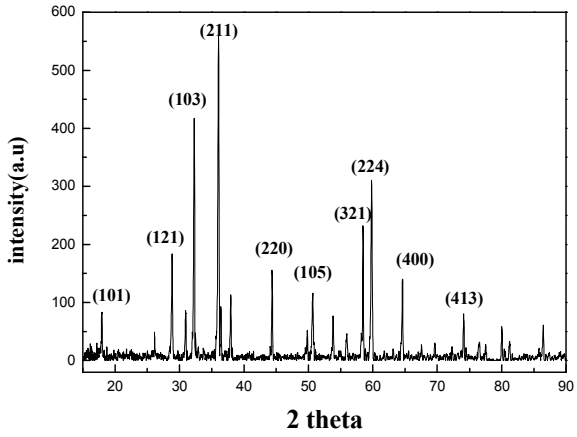

Fig. 1 XRD patterns of the as-prepared product

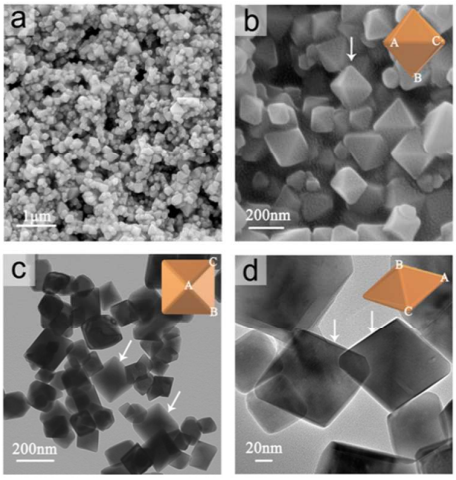

Fig. 2 A typical large-area SEM image (a) and a partially enlarged SEM image (b) of the Mn_3O_4 tetragonal bipyramids; A large-area TEM image (c) and an enlarged TEM image (d) of the Mn_3O_4 tetragonal bipyramids. The insets in b, c and d are the ideal geometrical models of the Mn_3O_4 tetragonal bipyramids marked with the corresponding white arrows, in which the ratio of AB and BC is about 1.1.

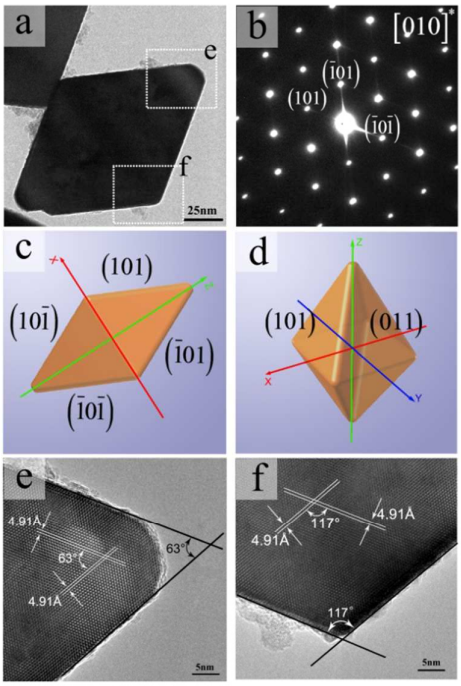

Fig. 3 (a) A typical TEM image of the Mn_3O_4 tetragonal bipyramids; (b) the corresponding selected area electron diffraction (SAED) pattern; (c) the corresponding simulated 2D geometrical model image along the Y axis; (d) The corresponding 3D geometrical model image; (e) a HRTEM image of the white rectangle marked with e in (a), the angle between two opposite planes is 63°; (f) a HRTEM image of the white rectangle marked with f in (a), the angle between two adjacent planes is 117°.

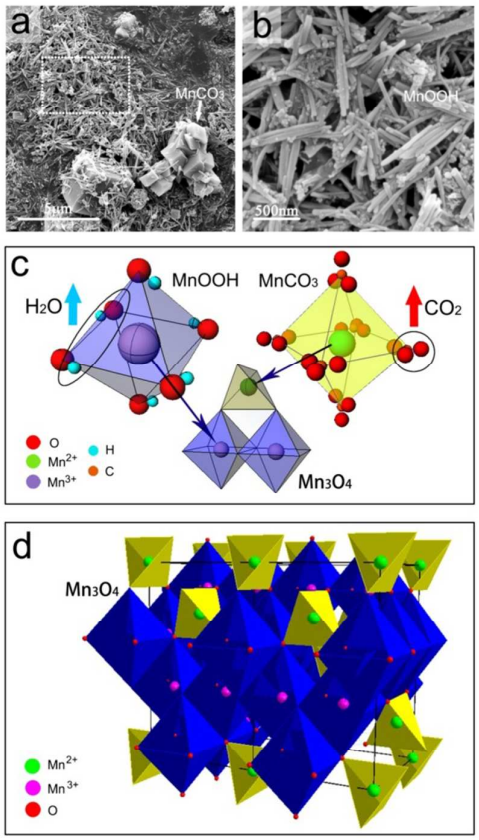

Fig. 4 (a) A SEM image and (b) a partially enlarged SEM image of the reaction process at 4 h; (c) a schematic illustration of the formation of the Mn_3O_4 tetragonal bipyramids transformed from $MnCO_3$ and MnOOH; (d) the crystal structure of the tetragonal Mn_3O_4 with two unit cells. The simulated diagrams of $MnCO_3$, MnOOH and Mn_3O_4 were extracted from the crystal files 1011262.cif, 9007689.cif, and 9009774.cif.

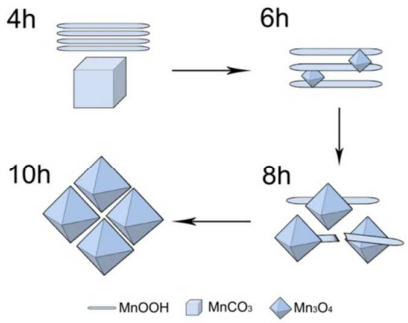

Fig. 5 A schematic illustration of the formation of the Mn_3O_4 tetragonal bipyramids.

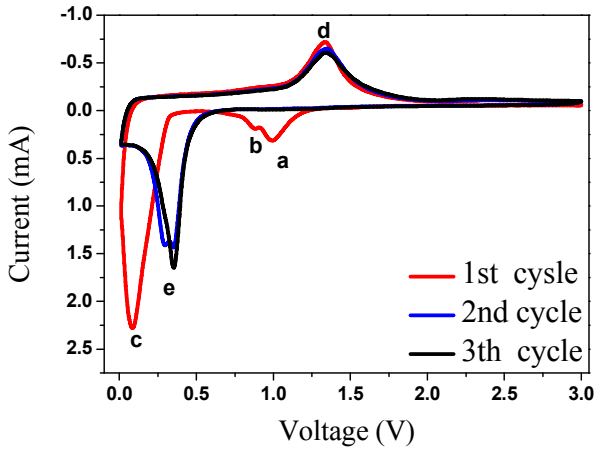

Fig. 6 CV curves of the Mn_3O_4 tetragonal bipyramid electrode at a constant density of 0.2 C in the voltage range 0.01 - 3.0 V. The number a, b, c, d and e denote the peaks.

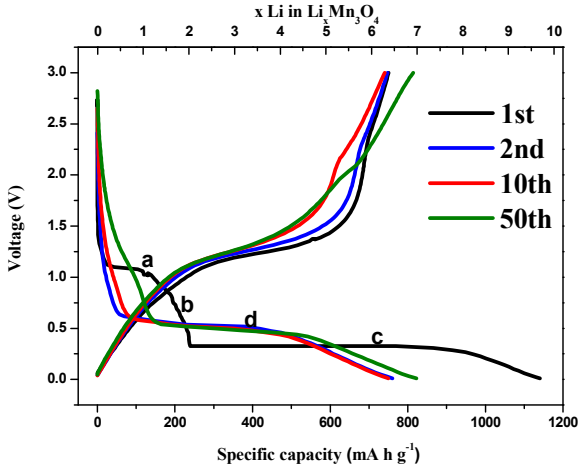

Fig. 7 The 1st, 2nd, 10th and 50th charge and discharge curves of the Mn_3O_4 tetragonal bipyramid electrode between 0.01 and 3 V at a current density of 0.2 C. The number a, b, c and d represent the plateaus and the sloped regions.

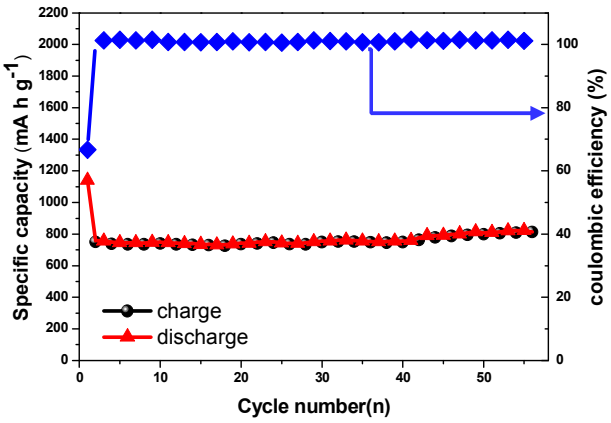

Fig. 8 Cycle performance and columbic efficiency versus cycle number of the Mn_3O_4 tetragonal bipyramid electrode at a current density of 0.2 C.

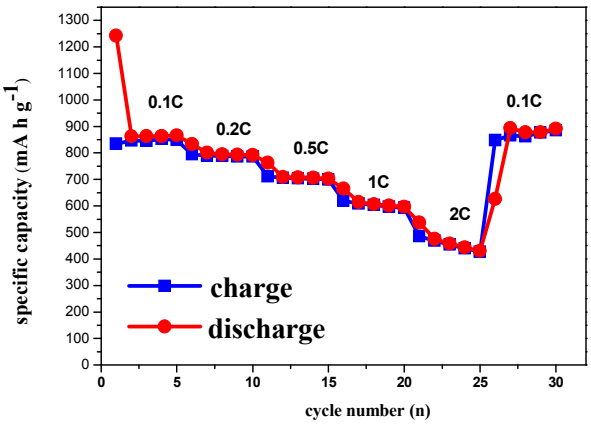

Fig. 9 The rate performance of the tetragonal bipyramid Mn_3O_4 electrode (rate= 0.1 - 2 C) and the cell was tested for 5 cycles at each current density.

Abstract:

Well-shaped Mn_3O_4 tetragonal bipyramids with a high reversible capacity of 822.3 mA h g^{-1} are synthesized by a simple hydrothermal method without any surfactants or coordination compounds. The structural feature and morphology of the final product are investigated by X-ray diffraction, scanning electron microscopy (SEM) and high-resolution transmission electron microscopy (HRTEM). The SEM and HRTEM results reveal that all eight exposed facets of the Mn_3O_4 tetragonal bipyramids are indexed to the high-energy {101} planes. The tetragonal bipyramids with high-energy facets provide Mn_3O_4 anode material with high initial discharge capacity (1141.1 mA h g^{-1}). In addition, the anode displays good fast rate performance, delivering a reversible capacity of 822.3 mA h g^{-1} (the theoretical capacity: 937 mA h g^{-1}) at a current density of 0.2 C after 50 cycles. And the coulomb efficiency for the first cycle reaches about 66% and remains at about 100% during the subsequent cycles. A relatively detailed growth mechanism of these tetragonal bipyramids is proposed in this manuscript.